Nanoscale Advances

ROYAL SOCIETY OF CHEMISTRY

PAPER

View Article Online
View Journal | View Issue

Cite this: *Nanoscale Adv.*, 2025, **7**, 6915

Heavy boron doping effects on biaxially tensile strained germanium (>1.5%) investigated *via* structural characterization, effective lifetime assessment and atomistic modeling

Shuvodip Bhattacharya, [a] Steven W. Johnston [b] and Mantu K. Hudait *[a]

Highly tensile strained germanium (ε-Ge) represents an essential material system for emerging electronic and photonics applications. Moreover, adjusting the doping levels to moderate or high concentrations can effectively tailor the properties of ε-Ge for specific applications. This article combines experimental characterization with a theoretical framework to examine the effects of heavy elemental boron (B) doping on pseudomorphic sub-50 nm ε-Ge. High resolution X-ray diffractometry is used to validate tensile strain levels of 1.53% and 1.68% in Ge epilayers, surpassing the indirect-to-direct band gap crossover point at ∼1.5% biaxial tensile strain. Cross-sectional transmission electron microscopy revealed visual evidence of stacking faults and surface roughening in 1.68% ε-Ge, although a coherent and abrupt Ge/III–V heterointerface is observed, devoid of interfacial misfit dislocations. Effective lifetime measurements demonstrated approximately twofold enhancement in 1.53% B-doped ε-Ge (N_B ∼7 × 10^{19} cm^{-3}) compared to its unstrained B-doped counterpart, while no such improvement was observed in 1.68% B-doped ε-Ge. This lack of enhancement is attributed to the presence of stacking faults and surface roughness within the ε-Ge epilayer. Through density functional theory calculations, we independently demonstrate that substitutional B atoms induce local deformation of Ge–Ge bonds in both unstrained Ge and ε-Ge epilayers, resulting in an additive tensile strain. This phenomenon could potentially lead to dynamic reduction and overcoming of the critical layer thickness for the system, facilitating the nucleation and subsequent glide of 90° leading Shockley partial dislocations, thereby generating stacking faults. In essence, these findings establish an upper limit on the B-doping concentration that can be achieved in highly ε-Ge epilayers, and collectively, offer valuable insights into the significance of heavy doping in Ge-based heterostructures. As such, this study delineates a fundamental constraint for integrating heavily doped ε-Ge in high-performance optoelectronic systems, necessitating precise strain-doping co-optimization to avoid performance degradation.

Received 28th April 2025
Accepted 9th September 2025

DOI: 10.1039/d5na00414d

rsc.li/nanoscale-advances

1. Introduction

The scope of application of heavily doped $Si_{1-x}Ge_x$, Ge, and $Ge_{1-y}Sn_y$ thin films is immense, and it should come as no surprise that these material systems have garnered special attention over the past decade. In addition to their significance in advancing complementary metal-oxide-semiconductor (CMOS) technologies,[1,2] this Group-IV trio forms part of a collective endeavor by researchers to enable monolithic integration of optical and photonic devices together with CMOS integrated circuits.[3–5] Furthermore, recent research has shown enormous potential of these material systems for application in spintronics,[6] quantum information processing,[7,8] particle detection,[9] optical sensing[10] and single-hole/single-electron transistors.[11] Particularly, holes in Ge exhibit strong inherent spin–orbit coupling and find application in hybrid semiconductor–superconductor hybrid systems. Moreover, Ge exhibits a pseudo-direct bandgap which can be engineered to become a direct band-gap material by virtue of uniaxial/biaxial tensile strain,[12–14] heavy *n*-type doping, Sn alloying[15] and special nanostructures such as nanomembranes[16] and micro-disks.[17,18] Such versatility opens up new frontiers in realizing Ge based optical sources to alleviate the performance limits of copper-based interconnect systems.[19–21] In all of the abovementioned applications, lattice engineering to induce strain and/or moderate to heavy doping concentrations are common factors to tailor the material system to specific applications. Previous investigations have focused primarily on (i) achieving heavily doped $Si_{1-x}Ge_x$[22] and Ge[23,24] epitaxial layers with high dopant

[a]*Advanced Devices & Sustainable Energy Laboratory (ADSEL), Bradley Department of Electrical and Computer Engineering, Virginia Tech, Blacksburg, Virginia 24061, USA. E-mail: mantu.hudait@vt.edu; Tel: +1 540-231-6663*

[b]*National Renewable Energy Laboratory, Golden, Colorado 80401, USA*

activation levels,[25] (ii) solid solubility limit of dopants in Ge,[23] (iii) magnetotransport properties of bulk/bulk-like Ge materials[26,27] and (iv) structural implications of heavy B-doping concentration in unstrained Ge.[28,29] However, not much work has been devoted toward understanding the implications of high concentrations of B-doping on ε-Ge beyond the crossover point, crucial for realizing the potential of such a material system in emerging technologies.

In this work, we employ a combination of structural characterization and effective lifetime measurements, independently corroborated using atomistic modeling, to investigate the impact of substantial B-doping on Ge epilayers, which are biaxially tensile strained above the crossover point.[30] Pseudomorphic unstrained Ge and tensile strained Ge (ε-Ge) were grown using solid-source molecular beam epitaxy (MBE) in isolated chambers. *In situ* B-doping was used to achieve a high concentration of B incorporation ($N_B \sim 7 \times 10^{19}$ cm^{-3} confirmed *via* Hall measurements) in the ε-Ge epilayers. High resolution X-ray analysis was employed to confirm strain levels of 1.53% and 1.68%. Using high-resolution cross sectional transmission electron microscopy, we show that heavy B-doping in highly ε-Ge favors formation of Shockley partial dislocations (SPDs) and surface roughness. Quantifiable corroboration with structural analysis is provided by way of micro-wave reflectance photoconductance decay effective minority carrier lifetime (τ_{eff}) measurements, where B-doped 1.53% ε-Ge showed ∼2× enhancement in τ_{eff} compared to its B-doped unstrained counterpart, while no such improvement in τ_{eff} was observed in B-doped 1.68% ε-Ge. This is attributed to the presence of stacking faults and induced surface roughness. These findings indicate an interplay of dynamics between tensile strain-induced (heavy doping-induced) lifetime enhancement (degradation), wherein enhancement in τ_{eff} is observed when the former dominates. Furthermore, atomistic modeling of B-doped bulk Ge and ε-Ge revealed that randomly distributed substitutional B-atoms induce deformation of Ge–Ge bonds, which result in an additive tensile strain, with the maximum exerted strain being possible at the Mott separation. The consequence is an inherent lowering of the critical layer thickness, h_c, for the system. When the h_c is exceeded, the cumulative tensile strain from the III–V strain template and substitutional B atoms paves the way for nucleation and glide of 90° leading to SPDs and formation of stacking faults. Thus, we speculate on the existence of a doping dependent critical tensile strain, ε_{doping}, beyond which surface roughening and nucleation of dislocations will compete, and might even become unavoidable, during epitaxial growth. For this work, the results suggest ε_{doping} exists between 1.53% and 1.68% tensile strain levels in ε-Ge for a B-doping concentration of $N_B \sim 7 \times 10^{19}$ cm^{-3}.

2. Experimental

2.1. Materials synthesis

In situ heavily B-doped ε-Ge heterostructures studied in this work were grown on epi-ready, semi-insulating GaAs (001) substrates with typical 2° ⟨110⟩ offcut, in an isolated group III–V and group IV dual-chamber solid-source MBE system. The chambers are interconnected *via* an ultra-high vacuum transfer chamber to prevent unwanted oxidation during transfer. The isolation is intended to mitigate atomic interdiffusion at group IV/group III–V heterointerfaces during epitaxial growth of group IV material at elevated temperatures. Growth temperatures at each stage were monitored using thermocouple and controlled using remotely calibrated Eurotherm 2404/8 PID controllers. Surface oxide desorption from GaAs substrates was performed at ∼750 °C with an As_2 overpressure of 10^{-5} Torr inside the III–V chamber to prevent surface reconstruction due to As desorption. A reflection high-energy electron diffraction (RHEED) module housed inside the III–V chamber was used for *in situ* monitoring of growth rate and temporal surface morphology variations at each growth stage. Oxide desorption step was concluded when clear (2 × 4) pattern was visible for each growth run. After oxide desorption, the substrates were cooled down to 650 °C for 250 nm of GaAs overgrowth. For the control heterostructure C, post GaAs overgrowth, 170 nm of AlAs was grown at 650 °C, following which the sample was transferred to the group IV chamber. For heterostructures A and B, after oxide desorption, $In_xGa_{1-x}As$ linearly graded metamorphic buffers (LGBs) were grown at 525 °C and 560 °C, respectively, where x was linearly varied by adjusting the cell temperature (or in other words, the In and Ga flux ratio) to achieve the desired InAs compositions for the respective buffers. A much thinner LGB was made possible in heterostructure A compared to heterostructure B by the overshoot layer, which promotes enhanced relaxation of the buffer, thereby providing a coherent growth front for the subsequent constant composition virtual substrate (VS) growth. Afterwards, constant composition $In_xGa_{1-x}As$ VSs were grown at 525 °C and 560 °C, respectively, for heterostructures A and B, at nominal growth rates of 0.6568 μm h^{-1} and 0.6951 μm h^{-1}. Finally, both samples were transferred to the group IV chamber under high vacuum. For heterostructure C, 270 nm epitaxial Ge, and for heterostructures A and B, ∼30 nm epitaxial Ge was grown, at a temperature of 400 °C at a nominal growth rate of 0.067 Å s^{-1}. The thickness for ε-Ge is limited by h_c in accordance with the strain energy balance model proposed by People and Bean.[31] To achieve the same doping concentration in all heterostructures, the B-dopant cell was maintained at 1650 °C during epitaxial Ge growth to achieve a B-doping concentration of $\sim 7 \times 10^{19}$ cm^{-3} (validated *ex situ* using Hall measurements on van der Pauw structures). After epitaxial Ge growth, all heterostructures were cooled down to 50 °C at a temperature ramp down rate of 5 °C min^{-1} to prevent thermal cracking or wafer bowing that could arise from the varying thermal coefficients of the materials used in the heterostructure stack. The heterostructures studied in this work are depicted in Fig. 1.

2.2. Materials analysis

To investigate the strain state of the Ge epilayers and InAs molar fraction in the $In_xGa_{1-x}As$ VSs, *ex situ* high-resolution X-ray diffraction (HR-XRD) was used. High resolution symmetric (004) and asymmetric (115) reciprocal space maps (RSMs) were recorded on a PANalytical X'Pert Pro diffractometer, which is

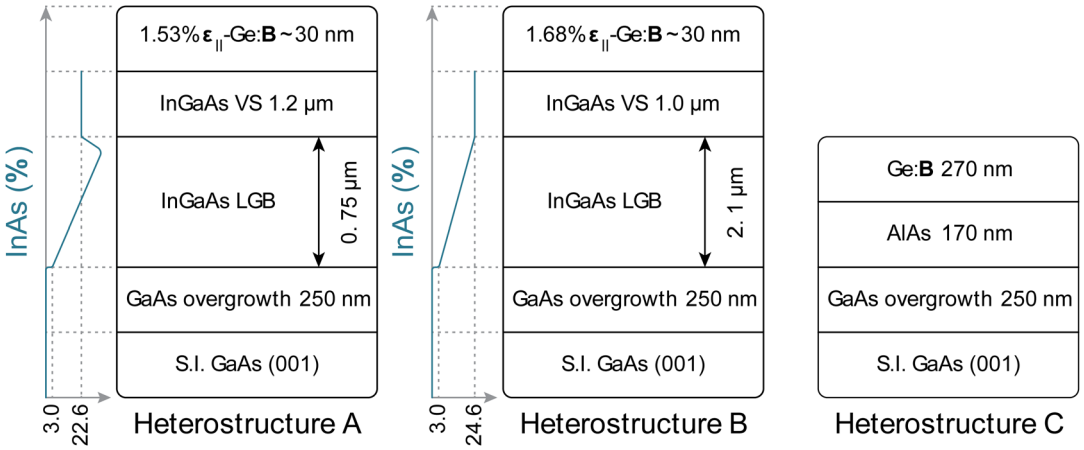

Fig. 1 Schematic representation of the heterostructures analyzed in this study. Heterostructure C serves as the unstrained control sample with 270 nm epitaxial Ge on vicinal 2° ⟨110⟩ (001) GaAs substrates with AlAs as an intermediate buffer. For heterostructures A and B, respectively, ~30 nm of 1.53% and 1.68% biaxially tensile strained epitaxial Ge was grown on InGaAs virtual substrates. The boron doping concentration for all heterostructures was confirmed *via* Hall measurements of van der Pauw structures to be $N_B \sim 7 \times 10^{19}$ cm^{-3}.

equipped with a monochromatic Cu Kα_1 ($\lambda = 1.540597$ Å) X-ray source. All RSMs were recorded with the PIXcel 3D detector, with the goniometer resolution set to 0.0001° and step size set to 0.0049° for both the 2θ and ω axes during measurement. To evaluate the structural implications of heavy B-doping on the ε-Ge epilayers and the ε-Ge/In$_x$Ga$_{1-x}$As heterointerfaces, bright field high-resolution cross sectional transmission electron micrographs (HR-XTEM) were recorded on a JEOL 2100 system with a formatted operating voltage of 200 kV ($\lambda_{electron}$ ~2.5079 pm). The electron transparent thin foils required for TEM characterization were prepared using conventional mechanical milling process, which was followed by Ar^+ ion milling at low temperatures to achieve the desired lamella. To measure the effective minority carrier lifetime of each B-doped sample, conventional (μ-PCD) measurements were performed at the National Renewable Energy Laboratory (NREL). All measurements were done at room temperature on representative 1 cm × 1 cm cleaved sample pieces. The samples were placed underneath a rectangular waveguide (WR42, 20 GHz, 0.43 cm × 1.07 cm) and optically pumped using a Q-switched neodymium-doped YAG laser with a power rating of 20 mW. The waveguide is used to guide the 20 GHz microwave probe source reflected from the samples that is recorded by an oscilloscope to map the conductance decay. The wavelength was maintained at 1500 nm for all measurements to ensure complete excitation of the Ge epilayers. The decay curves thus recorded were fitted with an exponential decay regression as explained in the later part of the text.

Atomistic density functional theory calculations were performed to study the deformation of Ge–Ge bonds in relaxed, undoped and B-doped 110 biaxially 1.5% ε-Ge. These calculations were made possible using the Synopsys QuantumATK software suite.[32] The standard unpolarized generalized gradient approximation (GGA)[33] with PerdewBurkeErnzerhof (PBE) exchange and correlation functionals was used for these calculations. Norm-conserving SG15 (ref. 34) pseudopotentials were used as the basis set for each element, with HighProjectorShift applied for Ge for reasons explained elsewhere.[32] Undoped and B-doped bulk and tensile-strained Ge supercells were geometrically optimized using a kinetic energy cutoff of 85 Hartree and a 6 × 6 × 8 Monkhorst–Pack k-point grid leading to 148 k-points to map the irreducible Brillouin zone, in conjunction with a force tolerance of 0.0005 eV Å^{-1}, stress error tolerance of 0.1 GPa and maximum allowed atomic displacement size of 0.2 Å.

3. Results and discussions

3.1. ε-Ge strain state and buffer InAs composition analysis using HR-XRD

The structural analyses of the heterostructures illustrated in Fig. 1 were conducted using double-axis HR-XRD. A typical combination of symmetric (004) and asymmetric (115) reciprocal space maps (RSMs) were recorded from each heterostructure to determine the InAs molar fraction in the InGaAs VS and the level of imparted mechanical strain to the active Ge epilayer, following methodologies outlined elsewhere.[35] In a typical symmetric (004) RSM along the (001) growth direction, the relative positions of the reciprocal lattice contour centroids (RLCCs) in relation to the substrate RLCC provide insights into the out-of-plane lattice parameters, $a_\perp$, of the corresponding epilayers. The RLCCs from individual epilayers in a symmetric scan should exhibit vertical alignment with the substrate along the Q_x axis, barring any influence from tilt or finite crystal effects.[36] However, in mismatched heteroepitaxy, strain relaxation often leads to tetragonal distortion of the lattice, resulting in potential epilayer tilt in arbitrary directions, influenced by the number and efficiency of slip systems active during the relaxation process. Non-uniform relaxation, typically linked to differences in preferential nucleation and glide velocities of α and β dislocations with group-V- and group-III-terminated cores, respectively, manifests as a horizontal shift of the RLCCs of the epilayers relative to that of the substrate in both symmetric and asymmetric scans.[37]

Fig. 2a and b display the symmetric (004) RSMs for heterostructures A and B, respectively, where the angular $(2\theta - \omega)$ coordinates have been converted to reciprocal space coordinates (reciprocal lattice unit, *r.l.u.*). The RLCCs of the constant composition InGaAs VSs are positioned below that of the GaAs substrate, in accordance with expansion (contraction) of out-of-plane lattice constant, $a_\perp$ (in-plane lattice constant, $a_\parallel$). Along the same lines, the RLCCs from the Ge epilayers are seen to be shifted above that of the GaAs substrates, indicative of expansion (contraction) of $a_\parallel$ ($a_\perp$), with the magnitude of displacement indicating the strain imparted to the Ge epilayers. The contour visible under the InGaAs VS in Fig. 2(a) and (c) is contribution from the forward overshoot layer employed in heterostructure A to promote enhanced buffer relaxation, as shown in Fig. 1 (inflection in % of InAs along growth). The magnitude of the vertical displacement of the InGaAs VSs RLCCs correlates with the InAs molar fraction present in the InGaAs VSs. A similar argument holds for the Ge RLCCs; a larger vertical displacement relative to the GaAs substrate RLCC suggests a higher tensile strain, and *vice versa*. Notably, while the InGaAs VS RLCC for heterostructure B is vertically displaced further than in heterostructure A – indicating a higher InAs molar fraction and consequently a higher tensile strain – it is observed that the Ge epilayer RLCCs in both heterostructures exhibit similar displacement magnitudes relative to the GaAs substrate RLCC. This could imply that the Ge epilayers in both heterostructures exhibit comparable tensile strain. This observation could arise from several possibilities: (i) insufficient relaxation of the buffer, (ii) partial relaxation of the Ge epilayer, or (iii) epilayer tilt resulting from tetragonal distortion which obscures the actual RLCC position. Further understanding of this observation can be gained from the asymmetric (115) scan. It should also be noted that the symmetric and well-defined contours of the InGaAs VSs suggest that defects nucleating from mismatched heteroepitaxy were effectively confined within the linearly graded metamorphic buffers. Consequently, reduced propagation of threading dislocations (TDs) to the InGaAs VSs and the active Ge epilayers can be expected.

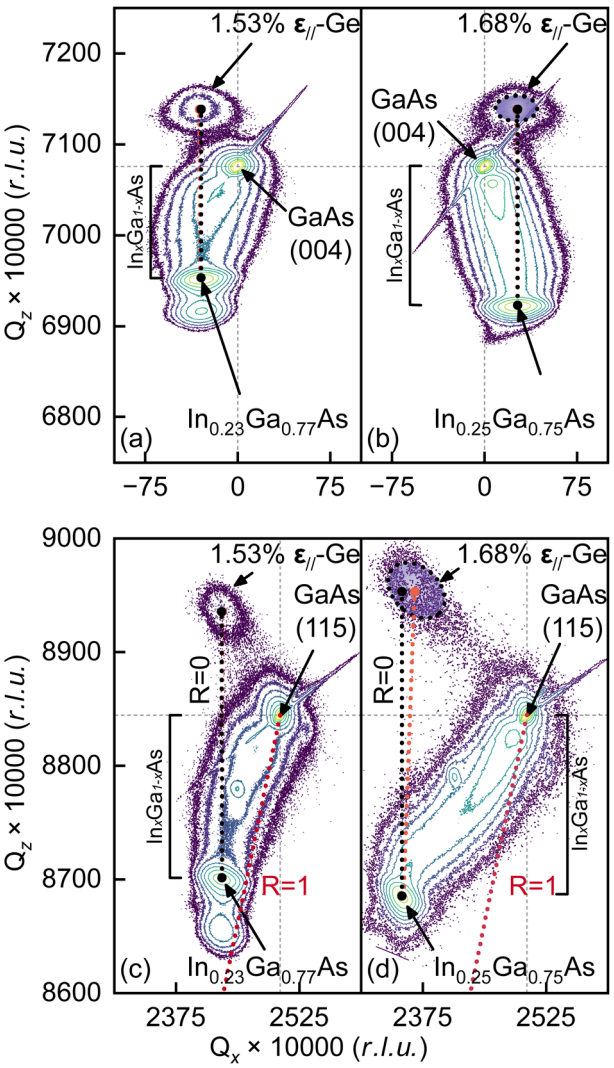

Fig. 2 (a and b) Symmetric (004) RSMs recorded from heterostructures A and B, respectively. The dotted orange lines connect the RLCC of the InGaAs VS and the ε-Ge epilayer used for characterization. The dotted black lines are provided to indicate the expected position of the Ge epilayer RLCC in the absence of tilt. (c and d) Asymmetric (115) RSM scans recorded from heterostructures A and B, respectively, with the dotted black and orange lines having the same significance as described previously. The dotted red line ($R = 1$) signifies the trajectory along which the InGaAs VS RLCCs would be position if they were fully relaxed.

As previously noted, crystallographic epilayer tilting relative to the substrate and between epilayers is often observed in mismatched heteroepitaxy. In Fig. 2, the reciprocal lattice contours (RLCs) from the respective epilayers exhibit horizontal shift relative to the GaAs substrate RLC due to epilayer tilting. Majority of the observed tilting occurs within the linearly graded metamorphic buffer, suggesting non-uniform relaxation dynamics,[37] whereas minimal tilt is observed between the InGaAs VS RLCC and the corresponding Ge epilayer RLCC. Illustrated as visual aids, the dotted orange lines are drawn from the InGaAs VS RLCCs and terminate at the corresponding Ge epilayer RLCCs utilized for tensile strain calculations. In contrast, the dotted black lines originate from the InGaAs VS RLCCs and extend to where the Ge epilayer RLCCs would coincide in the absence of tilt. The minimal angle between these two dotted lines in both heterostructures suggests minimal tilting; this finding rules out the possibility of partial relaxation in the Ge epilayer in heterostructure B. For heterostructure B specifically, due to the low intensity from the Ge epilayer contour, an ellipsoid is provided as visual aid to indicate the region of interest (ROI) used to locate the Ge RLCC.

To ascertain the out-of-plane lattice parameters, asymmetric (115) RSM scans were recorded from heterostructures A and B, as depicted in Fig. 2c and d. The low angle of incidence in an asymmetric scan results in additional splitting of the iso-intensity contours in the reciprocal coordinate space. Consistent with symmetric (004) scan findings, the InGaAs VS RLCCs are located below, and the Ge epilayer RLCCs are located above the GaAs substrate RLCCs. Notably, the Ge epilayer RLCC from heterostructure B is observed to be positioned slightly higher than that in heterostructure A. As mentioned earlier, tetragonal

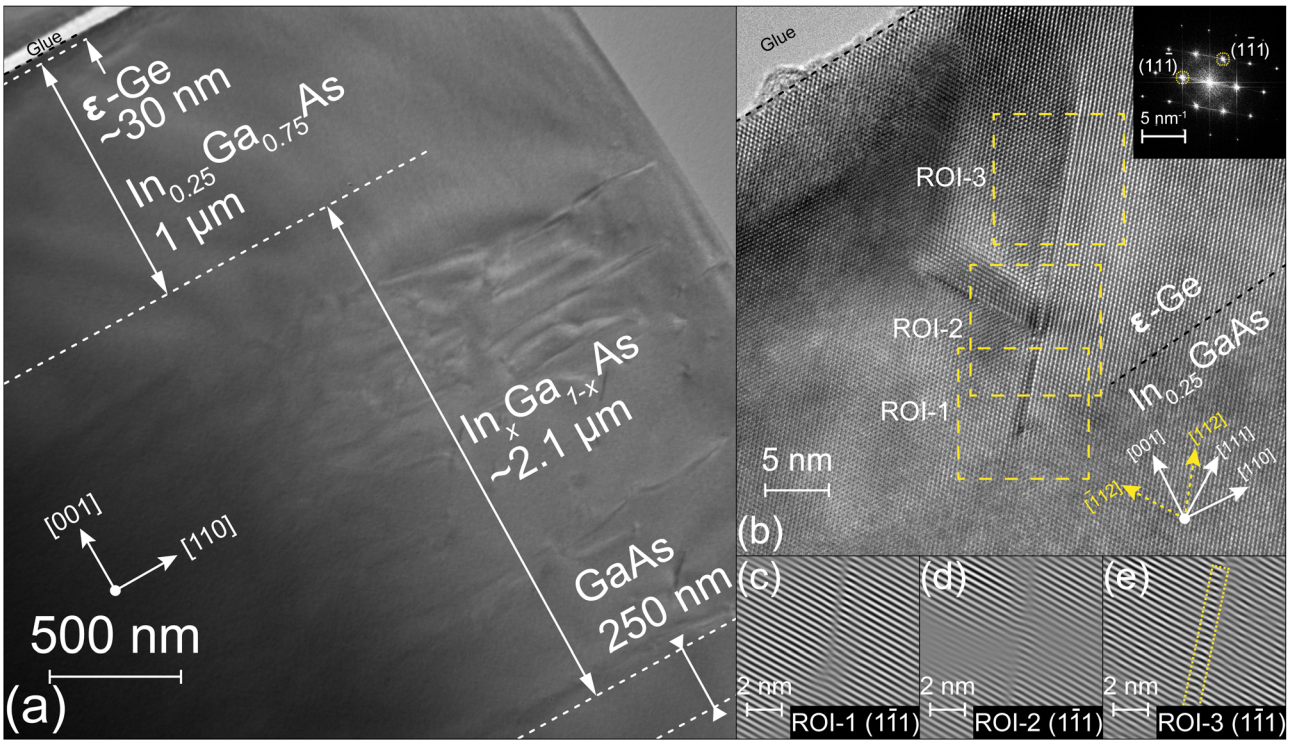

Fig. 3 (a) Cross-sectional low magnification bright-field TEM recorded heterostructure B showing the full stack. (b) High-resolution cross-sectional bright-field TEM recorded from heterostructure B, showing a representative ε-Ge/$In_{0.25}Ga_{0.75}As$ heterointerface region. The dotted yellow lines indicate the 10 nm × 10 nm regions of interest (ROIs) analyzed. The inset presents the FFT pattern derived from the entire region. The presence of an abrupt and coherent interface is evident by the difference in atomic factor contrast between Ge and $In_{0.25}Ga_{0.75}As$. A stacking fault is identifiable in this figure along the projected ⟨112⟩ directions. (c and e) Inverse FFT patterns corresponding to ROI-1, ROI-2 and ROI-3, respectively, obtained by selectively masking the (1$\bar{1}$1) planes from the FFT pattern displayed in the inset of (b). The dotted yellow line in (e) signifies the area of the two-monolayer twin observed in ROI-3.

distortion during mismatched heteroepitaxy may give rise to epilayer tilt which can obscure the accurate determination of the lattice parameters. Given the minimal epilayer tilting between the InGaAs VS and Ge epilayer RLCCs of interest, indicative of pseudomorphic growth, adjustments for epilayer tilt have not been pursued for this work. The nominal InAs compositions were determined to be 22.6% and 24.6% for heterostructures A and B, respectively, closely aligning with targets of 22.5% and 24%. We emphasize that the slight deviation between targeted and measured InAs molar fractions may be an artifact of epilayer tilt. The in-plane epitaxial strain, $\varepsilon_{\parallel}$, is defined as

$$\varepsilon_{\parallel} = \frac{a_{\parallel} - a_{r}}{a_{r}}, \quad (1)$$

where $a_{\parallel}$ and a_{r} refer to the in-plane lattice parameter and relaxed epilayer lattice parameter, respectively. Utilizing the relaxed lattice constant of Ge, $a_{r,Ge} = 5.658$ Å along with XRD measured in-plane lattice parameters, the strain states of Ge in heterostructure A ($a_{\parallel} = 5.7447$ Å) and heterostructure B ($a_{\parallel} = 5.7530$ Å) were calculated to be 1.53% and 1.68%, respectively, considering fully relaxed InGaAs virtual substrates. The calculated relaxed lattice parameters[35] for Ge were $a_{r,Ge} = 5.6583$ Å and $a_{r,Ge} = 5.6585$ Å, respectively, for heterostructures A and B, which are in close proximity to the literature value. Additionally, any minor discrepancy in the calculated relaxed Ge lattice parameter relative to the literature value for heterostructure B could be attributed to errors in locating the accurate RLCC position, considering the low intensity recorded. It is also important to note that while B-doping-induced tensile strain has been measured using HR-XRD previously,[38] decoupling the doping-induced tensile strain from mechanical strain induced by the metamorphic buffer presents significant challenges at this stage. This limitation arises from the fact that the ε-Ge unit cells are constrained by the underlying III–V strain template, where any alterations in the strain state due to B-induced distortion predominantly affect only the Ge–Ge bonds immediately proximal to the B atom. Consequently, such effect is likely obscured by the buffer-induced strain and exceeds the resolution capabilities of the current experimental setup.

3.2. Heterostructure analysis *via* TEM

To provide additional insight into the structural integrity of heavily *in situ* B-doped ε-Ge heterostructures in this work, cross-sectional low- and high-magnification TEM micrographs were recorded from heterostructure B. Fig. 3a illustrates the low-resolution cross-sectional TEM recorded from heterostructure B, displaying the complete stack. The lattice-mismatch induced defects are observed to be confined within the $In_xGa_{1-x}As$

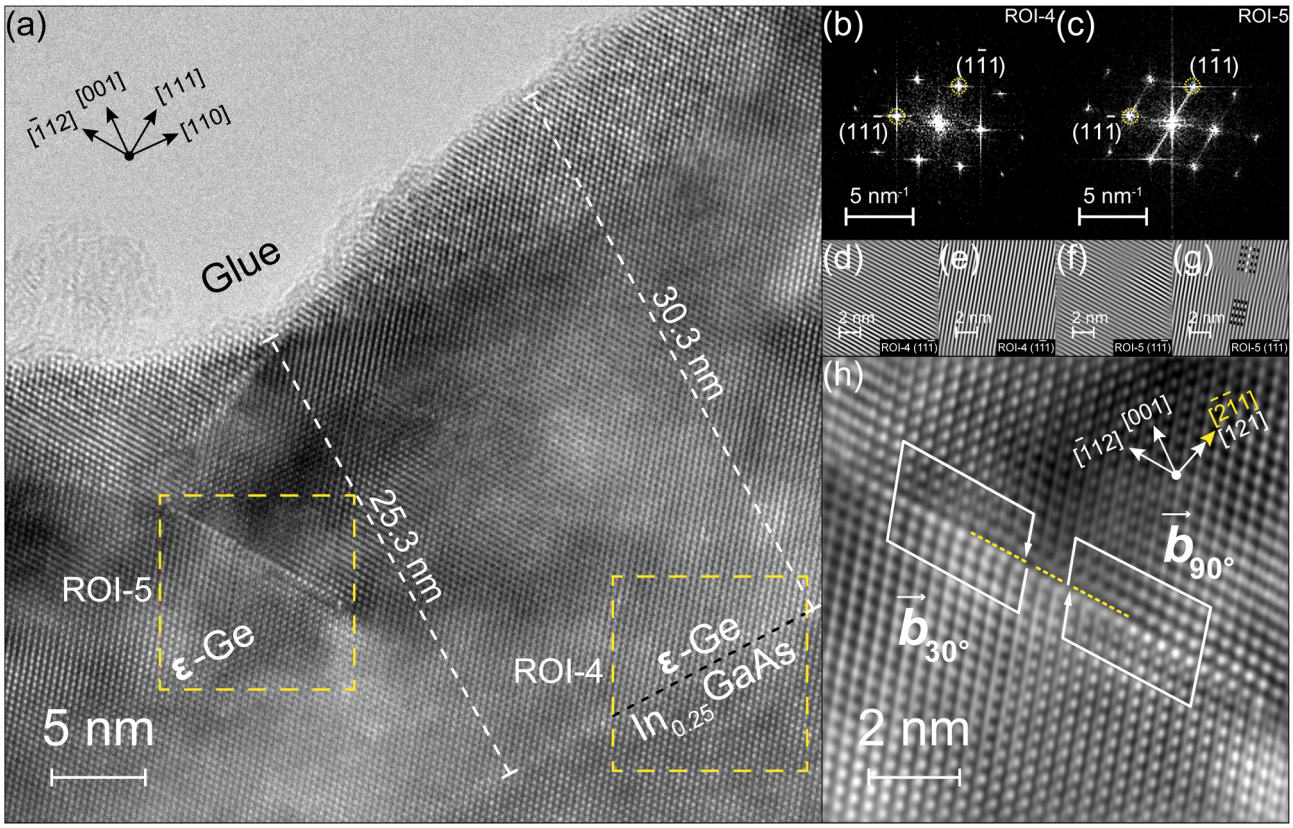

Fig. 4 (a) High-resolution cross-sectional bright-field TEM micrograph from a representative region of ε-Ge/$In_{0.25}Ga_{0.75}As$ heterointerface recorded from heterostructure B. The dotted yellow lines highlight the 10 nm × 10 nm ROIs analyzed. The variation in thickness, indicative of surface roughness, is represented by the dotted white lines, along with the corresponding measured thickness. (b and c) FFT diffraction patterns derived from ROI-4 and ROI-5, respectively. (d and e) Inverse FFT patterns from ROI-4, obtained by selectively masking (11$\bar{1}$) and (1$\bar{1}$1) diffraction points, respectively, with no lattice plane discontinuities observed. (f and g) Inverse FFT patterns from ROI-5, also obtained by selectively masking (11$\bar{1}$) and (1$\bar{1}$1) diffraction points, respectively, where lattice discontinuity is noted only along the (1$\bar{1}$1) planes, as indicated by the additional dotted white line. (h) Inverse FFT pattern obtained by mapping all diffraction points from ROI-5, clearly illustrating the stacking fault ribbon, with the 90° leading and 30° trailing PDs highlighted, as explained in the main text. The slip plane (1$\bar{1}$1) is marked by the dotted yellow line.

metamorphic buffer and do not glide into the constant composition InGaAs VS. This observation supports the previously noted symmetric and confined contours of the InGaAs VS in the recorded RSM. The absence of extended defects within the InGaAS VS and further into the active Ge epilayer suggests coherent pseudomorphic growth.

Fig. 3b presents a typical representative heterointerface region shared by the $In_{0.25}Ga_{0.75}As$ and ε-Ge. Several key observations can be made from this micrograph. The contrast in atomic factors between Ge and InGaAs highlights the abrupt nature of the heterointerface, indicating minimal atomic interdiffusion. Additionally, stacking faults are observed to initiate at the heterointerface (region of interest 1 (ROI-1)), and along the dislocation line, they dissociate into two 112 directions (ROI-2). The inset of Fig. 3b shows the diffraction pattern from the representative region, where diffraction streaks along the ⟨111⟩ directions suggest the presence of stacking faults. Moreover, the absence of satellite peaks in the diffraction pattern indicates that no multiple distinct lattice parameters exist, further confirming the pseudomorphic nature of the Ge epilayer.

In ROI-3, marked in the micrograph, a 2-monolayer twin region is identified, terminating at a SPD along the ⟨112⟩ direction. Using noise-filtering inverse Fast Fourier Transform (iFFT), selective masking of the (1$\bar{1}$1) planes from the diffraction pattern was conducted on ROIs 1, 2 and 3 as shown in Fig. 4c–e, respectively. Each figure reveals a discontinuity of lattice planes on the (1$\bar{1}$1) planes, with the 2-monolayer twin region highlighted by the yellow rectangular area in Fig. 3e. In contrast, no discontinuity was observed on the (11$\bar{1}$) planes (not shown here) indicating that the active slip plane in this case is either (1$\bar{1}$1) or (11$\bar{1}$).

Fig. 4a illustrates another representative heterointerface region shared between $In_{0.25}Ga_{0.75}As$ and ε-Ge from heterostructure B. Notably, this figure reveals a virtually defect-free heterointerface shared between the InGaAs VS and the active epitaxial Ge, as indicated by the dotted black line in ROI-4. Similar to the observations in Fig. 3b, the abrupt nature of the heterointerface is also evident here. In ROI-5, a stacking fault along the [$\bar{1}$12] direction is observed; however, unlike Fig. 3b, the stacking fault is located away from the heterointerface. This could suggest the presence of local micro-strain effects favoring

nucleation of partial dislocations (PDs) leading to stacking faults. Fig. 4b and c present the diffraction patterns obtained from ROIs 4 and 5, respectively. In these figures, satellite peaks are absent, reinforcing the pseudomorphic nature of the growth. Additionally, streaks are observed along the 111 directions, indicating the presence of the stacking fault. Fig. 4d–f depict the iFFT of selectively masked $(11\bar{1})$ and $(1\bar{1}1)$ diffraction points from ROIs 4 and 5, respectively. No discontinuity along the {111} planes is observed in ROI-4, which supports the presence of a coherent heterointerface. However, discontinuity in lattice planes is noted along the $(1\bar{1}1)$ planes from ROI-5, coinciding with the location of the identified stacking fault. Marée *et al.* have previously addressed that stacking faults are formed when the typical 60° mixed-type perfect dislocations in zinc blende structures (with Burgers vector $\frac{a}{2}\langle 110\rangle$) dissociate into pairs of SPD (with Burgers vector $\frac{a}{6}\langle 112\rangle$).[39] Under tensile shear stress, as is the case here, the maximum force is subjected to the 90° SPD which must nucleate first, followed by the trailing 30° SPD responsible for annihilating the stacking fault and restoring the typical ABCABC… stacking pattern along the $\langle 111\rangle$ directions observed in diamond cubic zinc blende structures. Fig. 4h displays the noise-filtered iFFT from the stacking fault region, notably showing clear evidence of a perfect 60° dislocation dissociating into a 90° leading SPD and 30° trailing SPD. A Burgers circuit is depicted around each SPD, with the plane of slip indicated by the dotted yellow line, surrounding the entire stacking fault ribbon. As discontinuity is observed on the $(1\bar{1}1)$ or $(\bar{1}1\bar{1})$ planes, projection of the Burgers vector onto the $(\bar{1}10)$ planes can infer the directions of the SPDs. Consequently, the dissociation of the perfect $\frac{a}{2}\langle 110\rangle$ dislocation is inferred as $\overrightarrow{b_{60^\circ}} \rightarrow \overrightarrow{b_{90^\circ}} + \overrightarrow{b_{30^\circ}} \Rightarrow \frac{a}{2}[110] \rightarrow \frac{a}{6}[121] + \frac{a}{6}[21\bar{1}]$, where a denotes the lattice parameter.

It is essential to address the presence of stacking faults, in contrast to the lack of visible disorder at the heterointerface in Fig. 3b and 4a. Despite the observations here, we previously demonstrated excellent pseudomorphic uid-epitaxial Ge growth with up to 1.94% tensile strain on a similar strain template (albeit with higher InAs content), where no extended defects or stacking faults were observed, at the heterointerface or within the ε-Ge epilayer.[40] A significant distinction in this study is the intentional *in situ* heavy B-doping of the ε-Ge epilayer. While the $In_{0.25}Ga_{0.75}As$ was not doped, the B dopant shutter was opened during the epitaxial Ge growth. Previous studies have shown that during B-doping, the lattice of the host Ge experiences warping in the vicinity of the B-atoms.[41] In a subsequent subsection, we illustrate this effect through atomistic modeling of the tensile strained system. Nonetheless, it is important to note that while low doping concentrations may or may not favor nucleation of dislocations, increasing local micro-strains within the Ge epilayer occurs due to reduced B–B distance at heavier doping concentrations.

The adverse effects of heavy B-doping on the crystallinity of Si, whether epitaxially grown or using the seed method, have been documented. For instance, Miller *et al.* studied the introduction of edge dislocations due to substantial contraction of the Si lattice beyond a B-doping concentration of 8×10^{18} cm^{-3}.[42] Schwuttke utilized X-ray topography measurements to illustrate the presence of precipitates along the {111} planes which serve as significant micro-strain centers.[43] Recently, it was reported that the solid solubility of B in Ge is $\sim 5.5 \times 10^{18}$ cm^{-3} at 850 °C in single crystal Ge.[23] Additionally, a B concentration as low as 1% facilitated compressive strain compensation in $Si_{1-x}Ge_x$ crystals, enabling a higher Ge content incorporation without an increase in residual strain energy.[44]

Furthermore, Fig. 4a presents an intriguing observation that is less apparent in Fig. 3b. In contrast to the coherent and abrupt ε-Ge/$In_{0.25}Ga_{0.75}As$ heterointerface, the terminating surface of the Ge epilayer exhibits undulations, suggesting a rough surface, with thickness ranging from 25.3 nm to 30.3 nm in the representative micrograph. Researchers have established that surface roughening by way of island formation serves as an elastic deformation pathway for alleviating misfit-induced strain.[45] This surface roughening competes with dislocation nucleation, with surface roughening scaling as ε^{-4} compared to ε^{-1} for dislocation nucleation, where ε is the lattice misfit. In mismatched heteroepitaxy, the energy barrier to surface roughening is significantly lower for high misfit growths, allowing for partial relaxation of misfit strain by surface roughening. Conversely, a critical misfit, ε_0, exists below which dislocation nucleation is favored over surface roughening, resulting in misfit strain relief through nucleation of new dislocations or glide of preexisting dislocations. This reduction in misfit strain subsequently increases the energy barrier for surface roughening, enabling the growth to proceed with an atomically smooth growth front. We have recently demonstrated island-driven growth (or 3D Stranski–Krastanov mode of growth) in epitaxial Ge grown on $In_{0.53}Ga_{0.47}As$ and $In_{0.51}Al_{0.49}As$, which contain significantly higher InAs compositions than those utilized in this work.[46]

In light of the aforementioned discussion, we propose that heavy B-doping, as is the case in this work, may be the primary cause for the nucleation of SPDs, consequently leading to stacking faults and/or surface roughening. One qualitative hypothesis could be the following. When growth of Ge begins from the abrupt Ge/$In_{0.25}Ga_{0.75}As$ heterointerface, the B adatoms occupy certain host Ge lattice sites, inducing significant warping of the Ge–Ge covalent bonds proximal to the B atoms, especially when random distribution of B atoms results in distance between neighboring dopants to be at or near the Mott limiting separation, as discussed shortly. This concomitantly increases the local strain at the growth front. At lower concentrations, only a limited number of Ge–Ge bonds around the B atoms are deformed. However, heavy B doping reduces the B–B distance, potentially leading to long-range residual strain energy. This additional strain energy lowers the critical misfit, ε_0, thereby promoting surface roughening. As some strain energy is relieved elastically by surface roughening, the critical misfit, ε_0, is again elevated, pushing the system into a low misfit regime. Consequently, the strain energy reduction induced by surface roughening at the growth front also diminishes the barrier for nucleation of dislocations, especially PDs in this

case. Furthermore, this dynamic modification of the h_c for the system due to the added strain makes it energetically favorable for nucleation and glide of perfect or partial dislocations, thereby providing a qualitative explanation for the observed stacking faults within the ε-Ge film. In a more specific case, the lattice distortion due to B adatoms can induce formation of PDs at the heterointerface itself, which could explain the formation of stacking faults at the heterointerface observed in this work in the absence of misfit dislocations or extended defects from the underlying buffers. In tandem, we emphasize that there exists a certain critical limit of tensile strain for a corresponding doping concentration, $\varepsilon_{\text{doping}}$, above which surface roughening, and possibly the nucleation of dislocations, will be observed. It is to be noted that no B precipitates or B impurity segregation were observed at the resolution limit of the current experimental setup, which have been shown to induce surface roughening[47] and nucleation of dislocations. A direct consequence of extended defects in epitaxial layers is the degradation of minority carrier lifetime, which is the topic of the next subsection.

3.3. Effective minority carrier lifetime using μ-PCD

In the context of semiconductor materials, minority carrier lifetime serves as a critical figure of merit (FOM) for assessing material quality. The presence of defects and other irregularities in the active material can cause severe degradation of minority carrier lifetime by functioning as effective recombination centers.[48,49] Additionally, surface roughness contributes to this degradation; effectively, surface roughness increases the number of surface states per unit area which can also act as recombination centers.

In this work, we have employed non-contact optical μ-PCD technique to analyze the heterostructures under investigation.[50,51] A microwave laser pump source is employed to generate photocarriers within the sample. This causes a change in local concentration and enhancement in local conductance. With the optical source removed, the excess photocarriers return to equilibrium conditions through various recombination processes. This process leads to a decrease in non-equilibrium conductance, which can be monitored using a microwave probe source. A considerable portion of the generated photocarriers also recombine at surface states before they can diffuse into the material, indicating that a surface lifetime component is always present within the observed characteristics. Moreover, the pump wavelength can be adjusted to mitigate the effect of the surface states. Longer wavelengths possess greater skin depth, which allows for a high concentration of photocarriers generated further from the surface, effectively within the bulk of the material. Under low injection conditions, we can neglect non-linear recombination dynamics and express the inverse of the principal mode of decay lifetime, τ_{eff}, as a cumulative sum of the inverse bulk lifetime component (τ_{bulk}) and inverse surface lifetime component (τ_{S}) as:[52,53]

$$\frac{1}{\tau_{\text{eff}}} = \frac{1}{\tau_{\text{bulk}}} + \frac{1}{\tau_{\text{S}}}. \quad (2)$$

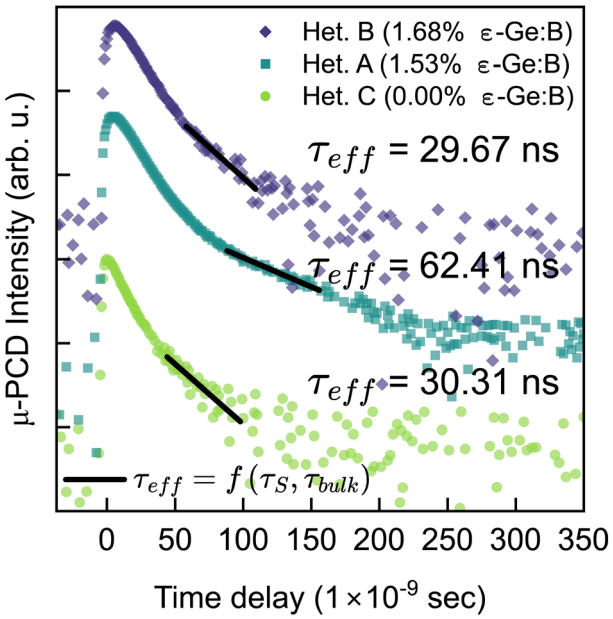

Fig. 5 Typical μ-PCD transient decay curves recorded from heterostructures (A), (B) and (C), as illustrated in Fig. 1. The effective minority carrier lifetime, τ_{eff}, is indicated for each trace. The traces have been normalized to the peak intensity and vertically shifted for clarity.

Fig. 5 presents typical μ-PCD transient decay curves obtained from the heterostructures illustrated in Fig. 1. According to theoretical studies, the crossover from indirect to direct band gap for biaxially ε-Ge occurs at ~1.5%,[30] where the fundamental direct band-gap is $E_g \sim 0.58$ eV ($\lambda \sim 2138$ nm). Consequently, we used $\lambda = 1500$ nm for the microwave pump source, ensuring that carriers are effectively excited to the fundamental L- and Γ-valleys across all heterostructures examined in this investigation. Furthermore, it is important to highlight that the underlying buffer layers are transparent at the selected wavelength, enabling us to exclusively probe the carrier dynamics within the Ge epilayers. For further details about the measurement technique, interested readers are encouraged to consult our previous works.[54,55]

The transient curves in Fig. 5 show an initial fast roll-off, which is attributed to the fast recombination at the surface states. Beyond the fast decay regime, the transient curves are dominated by the principal mode of decay. The effective lifetime, τ_{eff}, of the principal mode of decay was obtained using exponential decay regression according to $V_{\mu-\text{PCD}}(t) = V_0 \cdot e^{\left(-\frac{t}{\tau_{\text{eff}}}\right)}$, where $V_{\mu-\text{PCD}}$ is the temporal variation of the microwave probe source response (and is a direct measure of the change in local conductance), and V_0 is the peak microwave probe source intensity recorded at exactly time $t = 0$ s, or in other words, at the time when the optical source is removed. These findings are detailed in Table 1, which also includes previously reported experimentally measured τ_{eff} values from ε-Ge grown on InGaAs strain template for direct comparison.[54]

Table 1 Benchmarking effective minority carrier lifetimes of ε-Ge epilayers measured using microwave-reflection photoconductive decay (μ-PCD) technique

Sample	Ge (nm)	Ge strain (ε%)	Excitation wavelength (nm)	∼Photon fluence per pulse (photons per cm^2)	Doping concentration (cm^{-3})	μ–PCD lifetime (ns)	Fitting error (± ns)	Adjusted R^2 (unitless)
C	270	0.00	1500	1×10^8	B: $\sim 7 \times 10^{19}$	30.31	1.73	0.8798
A	∼30	1.53			B: $\sim 7 \times 10^{19}$	62.41	1.34	0.9719
B	∼30	1.68			B: $\sim 7 \times 10^{19}$	29.67	1.03	0.9537
R1 (ref. 54)	270	0.00			uid	95.37	0.19	0.9794
R2 (ref. 54)	75	0.61			uid	68.46	1.16	0.9509
R3 (ref. 54)	75	0.89			uid	89.75	1.68	0.9031
R4 (ref. 54)	30	1.60			uid	101.20	0.87	0.9817

A few notable insights can be drawn from Fig. 5. The τ_{eff} obtained from heterostructure A (1.53% ε-Ge) shows ∼2× improvement compared to heterostructure C, which is the control unstrained heavily B-doped Ge grown on GaAs, with AlAs as an intermediate buffer. This observation aligns qualitatively with our earlier reports, which indicate that pseudomorphic biaxially tensile strained Ge exhibits enhanced τ_{eff} compared to their unstrained counterparts, likely due to increased mobility induced by tensile strain.[56–58]

It is important to note that while higher doping may lead to higher impurity scattering rates and consequently affect mobility, the interplay between doping levels and tensile strain on mobility remains insufficiently understood at the present moment. As such, we believe this enhancement in τ_{eff} represents a cumulative effect of mobility degradation due to doping and mobility enhancement due to tensile strain, with the latter exerting a more significant influence. This conjecture is further supported by the lower τ_{eff} observed in heterostructure A compared to uid ε-Ge grown on InGaAs strain template reported previously (Samples R2–4 in Table 1). In fact, our uid unstrained Ge counterparts showed higher τ_{eff} than heterostructure C (Sample R1 in Table 1). Conversely, heterostructure B exhibits a reduction of ∼2× in τ_{eff} compared to heterostructure A, insofar that it exhibits a similar τ_{eff} as heterostructure C. This observation can be attributed to the presence of stacking faults in heterostructure B, which act as strong Shockley–Read–Hall (SRH) recombination centers, thereby degrading the τ_{bulk} component of τ_{eff}. Additionally, surface roughness seen in heterostructure B leads to additional surface states, which contribute to increased surface recombination. The resulting effect is an increased degradation in the τ_S component, in addition to the degraded τ_{bulk} in eqn (2), which ultimately results in a degraded effective minority carrier lifetime, τ_{eff}.

These observations provide substantial support for the findings presented in the XRD and TEM sections, as well as for the aforementioned hypothesis. Although heterostructure B has a slightly higher tensile strain than heterostructure A, the heavy B-doping affects the crystalline integrity of the material, concomitantly reducing the benefits of tensile strain. This ultimately reinforces the hypothesis that there exists a critical tensile strain corresponding to a specific doping concentration, $\varepsilon_{0,doping}$, below which the tensile strained-induced enhancement may be retained. While this relationship has not been explicitly calculated in this work, the findings suggest that $\varepsilon_{0,doping}$ likely falls between 1.53% and 1.68% tensile strain levels in this study.

3.4. Atomistic simulation for B-induced deformation of Ge–Ge bonds

In the current investigation, we have further employed atomistic density functional theory (DFT) calculations to study the structural deformation of Ge–Ge bonds resulting from the introduction of B dopant atoms under conditions of applied tensile strain. A relaxed Ge primitive cell was converted to a unit cell (8 atoms) using conventional transformation relevant to diamond cubic structures, followed by geometry optimization to obtain the energy minimized relaxed unit cell, with in-plane and out-of-plane lattice parameters equal to 5.736 Å.[32] To emulate the ∼1.5% ε-Ge/InGaAs heterostructure, a biaxial tensile [110] stress of 2.089 GPa was imposed on the relaxed energy minimized Ge unit cell during the geometry optimization step, yielding in-plane and out-of-plane lattice parameters of 5.814 Å and 5.661 Å, respectively. A change in the space group from orthorhombic (space group 227) to tetragonal (141) confirmed the tetragonal distortion of the structure under biaxial stress. A (001) oriented ε-Ge supercell was then constructed using the cell parameters determined from the strained Ge unit cell; within this structure, a singular Ge atom was replaced by a B atom. In adherence to periodic boundary conditions, the x and y dimensions of the supercell were set to $n \times a_{[110]}$, and z dimension was set to $(n-1) \times a_{[001]}$. Here, $n = 3$, $a_{[110]}$ is the lattice parameter in the x and y directions, and $a_{[001]}$ is the lattice parameter in the z direction. Geometry optimization was subsequently performed on the supercell while imposing constraints on the x, y and z directions, in order to accurately reflect the mechanical constraints exerted by the underlying III–V VS on the Ge film. The rationale to fix the lattice parameters of B-incorporated supercell prior to geometrical optimization can be justified as follows. The underlying InGaAs VSs are ∼0.75 μm and ∼2.1 μm in heterostructures A and B, respectively. It is assumed that the thin ∼30 nm epitaxial Ge film is mechanically constrained by the underlying stressors, and that, the proximal deformation of Ge–Ge bonds in the presence of dilute B dopant atoms is insufficient to induce long

range effects and revert this assumption at the Ge/III–V heterointerfaces.

To ascertain the deformation induced by B atoms, we adhered to the procedural methodology delineated in ref. 29. Illustrated in Fig. 6a is the representative supercell configuration of 1.5% ε-Ge, with $x = y = 3 \times a_{[110]}$ and $z = 2 \times a_{[001]}$, with an individual B atom incorporated into the central unit cell. This results in a periodic B–B distance, $d_{B\to B} = 12.365$ Å, which yields an effective B concentration of $\sim 6 \times 10^{20}$ cm^{-3}, about an order of magnitude larger than the experimental doping concentration. An increase in the volume of the supercell corresponds directly to augmentation of the B–B distance, or in other words, reducing B-dopant concentration within the Ge epilayer. We clarify that in the case of a periodic and homogeneous distribution of dopant atoms, $d_{B\to B} \approx 24.26$ Å at $N_B \sim 7 \times 10^{19}$ cm^{-3}, which differs significantly from the maximum supercell dimensions used in this work. Strictly speaking, this limits the direct quantitative extrapolation of the modeling results, reported here, to the lower experimental doping range. However, frequently DFT studies of dilute dopant atoms are approached with much higher concentrations than are typically observed (or achievable) in experiments, primarily due to the requirement of prohibitively large supercell sizes and the associated exceptional computational expense in modeling such material systems, especially when structural relaxation and electronic convergence is mandated. On the other hand, alternative to a periodic and homogeneous distribution of dopants is randomized distribution, in which case the limiting separation distance occurs at the Mott criterion for insulator-to-metal crossover. In that case, assuming a Poisson impurity distribution profile for the B-dopant atoms within the Ge epilayer, the B–B distance, $d_{B\to B}$, can be estimated as:[59]

$$d_{B\to B} \approx \frac{3}{2\pi} \cdot \frac{1}{\sqrt[3]{N_B}}. \quad (3)$$

Subsequently, for a doping concentration of $N_B \sim 7 \times 10^{19}$ cm^{-3} used in this work, $d_{B\to B} \approx 11.585$ Å according to eqn (3), which deviates by less than 1 Å of $d_{B\to B}$ of the simulated supercell dimensions depicted in Fig. 6a, along and normal to the growth direction. To circumvent the computational expense, we chose to utilize this limiting separation for modeling the effects of heavy B doping in ε-Ge.

The total volume of the supercell can be denoted as $V_{total} = N \cdot V_{cell}$, wherein N is the total number of unit cells incorporated in the supercell, and V_{cell} designates the volume of each discrete

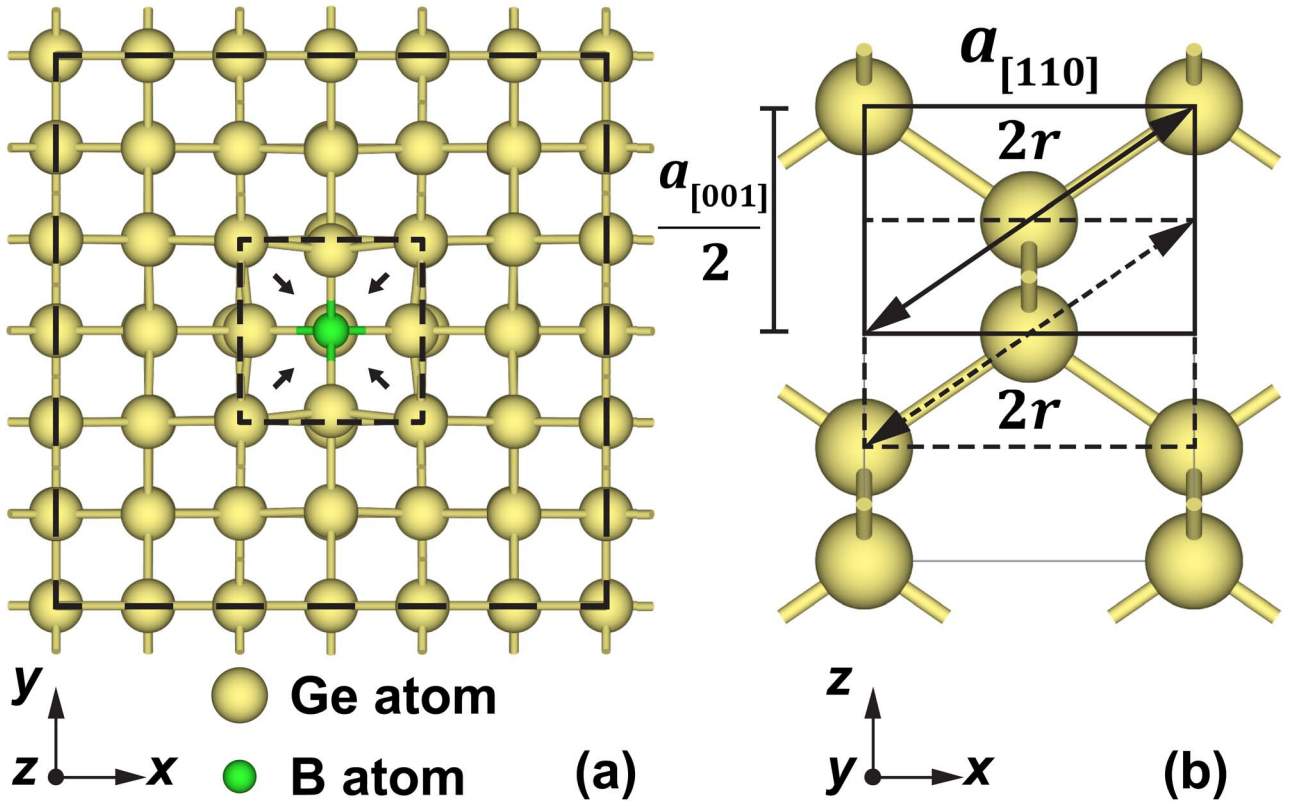

Fig. 6 (a) Depicts a representative supercell utilized for the atomistic modeling of B dopant atoms in a (001) oriented Ge. The dimensions of the supercell are defined as $x = y = 3 \times a_{[110]}$ and $z = 2 \times a_{[001]}$, to preserve periodic boundary conditions. The dotted black line illustrates one [110] oriented unit cell, each of which consists of either 4 Ge atoms, or 3 Ge atoms and 1 B atom. (b) Outlines the qualitative model employed for this study along the [001] direction, based on the assumption that $2r = \sqrt{a_{[110]}^2 + \left(\frac{a_{[001]}}{2}\right)^2} \approx \sqrt{a_{[110]}^2 + \left(\frac{a_{[110]}}{\sqrt{2}}\right)^2}$. The calculated changes in bond lengths are referenced against the geometry optimized undoped, unstrained bulk Ge.

unit cell. It is evident from Fig. 6a that the B-containing unit cell undergoes volumetric contraction attributable to the disparity in covalent radii between Ge and B. In a similar vein, given that the Ge epilayer is constrained by the III–V strain template, certain Ge–Ge bonds proximal to the B-containing unit cell undergo an effective expansion, which corresponds to an added tensile strain condition. Consequently, a rudimentary qualitative model may be employed to map the strain induced in the Ge–Ge bonds in the presence of substitutional B atoms. If we designate δ and γ, respectively, as proportional volumetric contraction and expansion coefficients, V_B and V_{Ge} as the volumes of B-containing unit cell and Ge-containing cells, respectively, V_{total} can be formulated as:[29]

$$V_{total} = V_B + (N-1)\cdot V_{Ge}, \quad (4)$$

$$V_B = \frac{V_{total}}{N}\cdot(1-\delta), \quad (5)$$

and,

$$V_{Ge} = \frac{V_{total}}{N}\cdot(1+\gamma). \quad (6)$$

Finally, Fig. 6b illustrates that the volume of each unit cell can be represented in relation to the Ge–Ge ($r_{Ge\rightarrow Ge}$) or Ge–B ($r_{Ge\rightarrow B}$) bond lengths as:

$$V_{Ge/B} = \frac{1}{\sqrt{2}}\cdot\left(\sqrt{\frac{8}{3}}\cdot r_{Ge\rightarrow Ge/Ge\rightarrow B}\right)^3. \quad (7)$$

Therefore, combining eqn (4)–(7), we get:

$$\delta = 1 - \frac{N}{\sqrt{2}V_{total}}\cdot\left(\sqrt{\frac{8}{3}}\cdot r_{Ge\rightarrow Ge/Ge\rightarrow B}\right)^3, \quad (8)$$

leading to:

$$\delta = (N-1)\cdot\gamma. \quad (9)$$

The values of $r_{Ge\rightarrow Ge}$ were obtained from geometry optimized cells of bulk Ge, 1.5% ε-Ge interface supercell and B-doped 1.5% ε-Ge interface supercell, as detailed in Table 2. An effective maximum additive tensile strain of 0.2854–0.2912% was identified in B-doped ε-Ge compared to undoped 1.5% ε-Ge, aligning closely with previously reported estimates within the constraints of atomistic modeling.[29] The provided range accounts for the variations in $r_{Ge\rightarrow B}$ due to the tetragonal distortion of the lattice induced by the tensile strain from underlying III–V buffer template, which leads to slight differences in $r_{Ge\rightarrow B}$ along the [110] and [001] directions. We emphasize here that while direct quantitative correlation cannot be established with the lower experimental doping concentration, the results of the modeling yield the upper ceiling of the additive tensile strain that can be imposed by the presence of B atoms in ε-Ge. On the corollary, B dopant atoms spaced further would then exert a lesser additive tensile strain, consistent with our earlier findings for heavily B-doped unstrained Ge.[29] Alternatively, the locations where a combination of the buffer-induced tensile strain and additive strain due to B atoms causes h_c to be exceeded, are the locations where nucleation of defects will occur. This conjecture is immediately supported by the observations made in Fig. 3 and 4; the lack of ordered defect nucleation alludes to randomized distribution of dopants, further corroborating the basis of the modeling pursued in this work.

Table 2 Summary of extracted parameters obtained from atomistic simulation of undoped and B-doped unstrained and tensile strained Ge supercells

Parameter	Extracted value (unit)
$r_{Ge\rightarrow Ge}$ (relaxed Ge bulk)	2.48483 Å
$r_{Ge\rightarrow Ge}$ (1.5% ε-Ge)	2.50079 Å
$r_{Ge\rightarrow Ge}$ (1.5% ε-Ge : B)	2.50804 Å
$r_{Ge\rightarrow B}$ (1.5% ε-Ge : B)	2.18951 Å
Contraction coefficient, δ	30.515%
Expansion coefficient, γ	0.872%

It is well established that nucleation of defects, by means of heterointerfacial misfit dislocations and gliding threading dislocations, becomes energetically favorable in mismatched heteroepitaxy when h_c is exceeded. To reiterate, while evidence of stacking faults is presented in Fig. 3b and 4a, no misfit dislocations were detected at the heterointerface. This observation suggests that the effective tensile strain, induced by the III–V strain template and heavy B doping, impedes the glide of 60° perfect dislocations. Instead, the dissociation of the perfect dislocations into their 90° PD component and their subsequent glide appears to be favored, resulting in the formation of stacking faults. Consequently, this indicates an inherent modification of the strain energy balance model, suggesting that a lower effective h_c is adequate to nucleate 90° PDs and stacking faults. Referring to the strain energy balance model by People and Bean,[31] 1.53% and 1.68% tensile strain levels, respectively, correspond to h_c of ~48 nm and ~38 nm. Given that the thickness of both Ge epilayers in this work is ~30 nm, it can be posited that the cumulative tensile strain from the III–V strain template, and that induced by the substitutional B atoms, leads to h_c being exceeded in heterostructure B. As a result, the nucleation and subsequent glide of 90° PDs becomes energetically favorable. This finding supports the observations made by XRD and TEM analyses and explains the origin of the stacking faults at the heterointerface and within the film. Furthermore, as τ_{eff} showed a twofold improvement in heterostructure A compared to heterostructure C, one can argue that the ε-Ge is pseudomorphic in heterostructure A and that the conditions for h_c to be exceeded for this system have not been met. Although we have not calculated the forces governing the nucleation and glide of 90° PDs in this study, prior research has documented such a phenomenon in strained epitaxy of silicon on Ge_xSi_{1-x} VSs, where a modified h_c for stacking fault generation was established.[60] Therefore, this work provides valuable insights and considerations regarding the impact of heavy B-doping of highly ε-Ge epilayers, which hold significant potential for various emerging electronic and photonic applications.

4. Conclusions

In summary, we have conducted a thorough investigation into the effects of heavy B-doping on highly ε-Ge, utilizing structural and effective lifetime characterization and independently validating the observations by atomistic modeling. We demonstrated successful growth of heavily B-doped 1.53% and 1.68% ε-Ge ($N_B \sim 7 \times 10^{19}$ cm^{-3} as confirmed by HR-XRD measurements). HR-XTEM analyses revealed a coherent and abrupt heterointerface between 1.68% ε-Ge and $In_{0.25}Ga_{0.75}As$ heterointerface, while also providing visual evidence of stacking faults and surface roughening. Measurement of effective lifetime *via* μ-PCD indicated that tensile strain induced an enhancement in τ_{eff} to 62 ns (up from 30 ns in unstrained highly B-doped Ge) in the 1.53% ε-Ge sample. However, no such improvement was observed in 1.68% ε-Ge, which we attribute to the presence of stacking faults and surface roughness within the Ge epilayer. Through independent first-principles atomistic calculations, we demonstrate that the deformation of Ge–Ge bonds due to substitutional B-atoms induces an additive tensile strain, with an upper ceiling established at the Mott criterion for dopant separation. This deformation effectively could lower the critical layer thickness, h_c, for the system, thereby energetically favoring the nucleation and subsequent glide of 90° leading PDs, which results in the formation of stacking faults. These stacking faults are primarily responsible for the degradation of τ_{eff} in the 1.68% ε-Ge sample. Consequently, this work highlights that while heavily B-doped ε-Ge can be achieved, it is essential to consider the structural implications of the same. Furthermore, this work provides a novel approach to achieving high tensile strain in Ge epilayers without necessitating higher InAs compositions in the underlying III–V strain template. Overall, this research provides a comprehensive understanding of ε-Ge:B/InGaAs material system, which will be beneficial for their application in emerging electronic and photonic applications.

Author contributions

Shuvodip Bhattacharya: conceptualization, data analysis, curation, atomistic modeling, investigation, visualization, writing – original draft, review, and editing; Steven W. Johnston: resources, lifetime data collection, investigation, writing – review and editing; Mantu K. Hudait: resources, supervision, project administration, methodology, analysis, writing – review and editing.

Conflicts of interest

There are no conflicts to declare.

Data availability

This research paper presents experimental findings, supported by density functional theory calculations using QuantumATK, and no external data was used to develop any conclusions. However, if any measurement or simulation data is required, those can be made available upon request from the corresponding author.

Acknowledgements

S. B. acknowledges contributions of Michael B. Clavel for overseeing and facilitating epitaxial growth of heterostructures, and Jheng-Sin Liu for recording TEM used in this work. M. K. H. acknowledges partial support from the NSF under grant numbers ECCS-2042079, a US-Ireland Joint R&D Program, and ECCS-2430393, as well as Virginia Tech Nanofabrication facilities for assistance during materials analysis. In addition, the Nanoscale Characterization and Fabrication Laboratory, which is funded and managed by Virginia Tech's Institute for Critical Technology and Applied Science, is used for the TEM measurement. S. J. acknowledges that the views expressed herein do not necessarily represent the views of the U.S. Department of Energy or the United States Government.

Notes and references

1 O. Qiqing, Y. Min, J. Holt, S. Panda, C. Huajie, H. Utomo, M. Fischetti, N. Rovedo, L. Jinghong, N. Klymko, H. Wildman, T. Kanarsky, G. Costrini, D. M. Fried, A. Bryant, J. A. Ott, I. Meikei and S. Chun-Yung, *2005 Symposium on VLSI Technology*, 2005 Digest of Technical Papers, 2005 pp. 28–29, DOI: 10.1109/.2005.1469199.
2 B. Liu, C. Zhan, Y. Yang, R. Cheng, P. Guo, Q. Zhou, E. Y. J. Kong, N. Daval, C. Veytizou, D. Delprat, B. Y. Nguyen and Y. C. Yeo, *IEEE Trans. Electron Devices*, 2013, **60**, 2135–2141.
3 E. Kasper, M. Oehme, T. Arguirov, J. Werner, M. Kittler and J. Schulze, *Adv. OptoElectron.*, 2012, **2012**, 916275.
4 G. T. Reed, G. Z. Mashanovich, F. Y. Gardes, D. J. Thomson, Y. Hu, J. Soler-Penades, M. Nedeljkovic, A. Khokar, P. Thomas, C. Littlejohns, A. Ahmad, S. Reynolds, R. Topley, C. Mitchell, S. Stankovic, P. R. Wilson, L. Ke, T. M. B. Masaud, A. Tarazona and H. Chong, *Proc. SPIE 8989, Smart Photonic and Optoelectronic Integrated Circuits XVI*, 2014, vol. 8989, p. 89890D, DOI: 10.1117/12.2045490.
5 J. Liu, *Photonics*, 2014, **1**, 162–197.
6 Y. Zhou, W. Han, L.-T. Chang, F. Xiu, M. Wang, M. Oehme, I. A. Fischer, J. Schulze, R. K. Kawakami and K. L. Wang, *Phys. Rev. B*, 2011, **84**, 125323.
7 G. Scappucci, C. Kloeffel, F. A. Zwanenburg, D. Loss, M. Myronov, J.-J. Zhang, S. De Franceschi, G. Katsaros and M. Veldhorst, *Nat. Rev. Mater.*, 2021, **6**, 926–943.
8 N. W. Hendrickx, W. I. L. Lawrie, M. Russ, F. van Riggelen, S. L. de Snoo, R. N. Schouten, A. Sammak, G. Scappucci and M. Veldhorst, *Nature*, 2021, **591**, 580–585.
9 K. Vetter, *Annu. Rev. Nucl. Part. Sci.*, 2007, **57**, 363–404.
10 R. R. Sumathi, N. Abrosimov, K.-P. Gradwohl, M. Czupalla and J. Fischer, *J. Cryst. Growth*, 2020, **535**, 125490.
11 P.-Y. Hong, C.-C. Lai, T. Tsai, H.-C. Lin, T. George, D. M. T. Kuo and P.-W. Li, *Sci. Rep.*, 2023, **13**, 14333.
12 B. Dutt, D. S. Sukhdeo, D. Nam, B. M. Vulovic, Z. Yuan and K. C. Saraswat, *IEEE Photonics J.*, 2012, **4**, 2002–2009.

13 D. S. Sukhdeo, D. Nam, J.-H. Kang, M. L. Brongersma and K. C. Saraswat, *Photon. Res.*, 2014, **2**, A8–A13.
14 M. K. Hudait, F. Murphy-Armando, D. Saladukha, M. B. Clavel, P. S. Goley, D. Maurya, S. Bhattacharya and T. J. Ochalski, *ACS Appl. Electron. Mater.*, 2021, **3**, 4535–4547.
15 E. Kasper, M. Kittler, M. Oehme and T. Arguirov, *Photon. Res.*, 2013, **1**, 69–76.
16 A. Gassenq, K. Guilloy, G. O. Dias, N. Pauc, D. Rouchon, J.-M. Hartmann, J. Widiez, S. Tardif, F. Rieutord, J. Escalante, I. Duchemin, Y.-M. Niquet, R. Geiger, T. Zabel, H. Sigg, J. Faist, A. Chelnokov, V. Reboud and V. Calvo, *Appl. Phys. Lett.*, 2015, **107**, 191904.
17 A. Ghrib, M. El Kurdi, M. Prost, S. Sauvage, X. Checoury, G. Beaudoin, M. Chaigneau, R. Ossikovski, I. Sagnes and P. Boucaud, *Adv. Opt. Mater.*, 2015, **3**, 353–358.
18 V. Reboud, A. Gassenq, N. Pauc, J. Aubin, L. Milord, Q. M. Thai, M. Bertrand, K. Guilloy, D. Rouchon, J. Rothman, T. Zabel, F. A. Pilon, H. Sigg, A. Chelnokov, J. M. Hartmann and V. Calvo, *Appl. Phys. Lett.*, 2017, **111**, 092101.
19 K. H. Koo, H. Cho, P. Kapur and K. C. Saraswat, *IEEE Trans. Electron Devices*, 2007, **54**, 3206–3215.
20 K. Saraswat, D. Kim, T. Krishnamohan, D. Kuzum, A. K. Okyay, A. Pethe and H.-Y. Yu, *ECS Trans.*, 2008, **16**, 3–12.
21 P. Chaisakul, D. Marris-Morini, J. Frigerio, D. Chrastina, M.-S. Rouifed, S. Cecchi, P. Crozat, G. Isella and L. Vivien, *Nat. Photonics*, 2014, **8**, 482–488.
22 J. Aubin, J. Hartmann, M. Veillerot, Z. Essa and B. Sermage, *Semicond. Sci. Technol.*, 2015, **30**, 115006.
23 S. Uppal, A. F. Willoughby, J. M. Bonar, A. G. Evans, N. E. Cowern, R. Morris and M. G. Dowsett, *J. Appl. Phys.*, 2001, **90**, 4293–4295.
24 T.-H. Chang, C. Chang, Y.-H. Chu, C.-C. Lee, J.-Y. Chang, I.-C. Chen and T. Li, *Thin Solid Films*, 2014, **551**, 53–56.
25 A. Satta, E. Simoen, T. Clarysse, T. Janssens, A. Benedetti, B. De Jaeger, M. Meuris and W. Vandervorst, *Appl. Phys. Lett.*, 2005, **87**, 172109.
26 P. J. Newton, J. Llandro, R. Mansell, S. N. Holmes, C. Morrison, J. Foronda, M. Myronov, D. R. Leadley and C. H. W. Barnes, *Appl. Phys. Lett.*, 2015, **106**, 172102.
27 M. B. Clavel, J.-S. Liu, M. A. Meeker, G. A. Khodaparast, Y. Xie, J. J. Heremans, S. Bhattacharya and M. K. Hudait, *J. Appl. Phys.*, 2020, **127**, 075702.
28 G. Zhou, K. H. Lee, D. H. Anjum, Q. Zhang, X. Zhang, C. S. Tan and G. Xia, *Opt. Mater. Express*, 2018, **8**, 1117–1131.
29 M. B. Clavel, G. Greene-Diniz, M. Grüning, K. T. Henry, M. Kuhn, R. J. Bodnar and M. K. Hudait, *ACS Appl. Electron. Mater.*, 2019, **1**, 2646–2654.
30 D. Saladukha, M. B. Clavel, F. Murphy-Armando, G. Greene-Diniz, M. Grüning, M. K. Hudait and T. J. Ochalski, *Phys. Rev. B*, 2018, **97**, 195304.
31 R. People and J. C. Bean, *Appl. Phys. Lett.*, 1985, **47**, 322–324.
32 S. Smidstrup, T. Markussen, P. Vancraeyveld, J. Wellendorff, J. Schneider, T. Gunst, B. Verstichel, D. Stradi, P. A. Khomyakov, U. G. Vej-Hansen, M.-E. Lee, S. T. Chill, F. Rasmussen, G. Penazzi, F. Corsetti, A. Ojanperä, K. Jensen, M. L. N. Palsgaard, U. Martinez, A. Blom, M. Brandbyge and K. Stokbro, *J. Phys.: Condens. Matter*, 2020, **32**, 015901.
33 M. A. L. Marques, M. J. T. Oliveira and T. Burnus, *Comput. Phys. Commun.*, 2012, **183**, 2272–2281.
34 M. Schlipf and F. Gygi, *Comput. Phys. Commun.*, 2015, **196**, 36–44.
35 J.-M. Chauveau, Y. Androussi, A. Lefebvre, J. D. Persio and Y. Cordier, *J. Appl. Phys.*, 2003, **93**, 4219–4225.
36 G. Bauer, J. Li and E. Koppensteiner, *J. Cryst. Growth*, 1995, **157**, 61–67.
37 K. L. Kavanagh, M. A. Capano, L. W. Hobbs, J. C. Barbour, P. M. J. Marée, W. Schaff, J. W. Mayer, D. Pettit, J. M. Woodall, J. A. Stroscio and R. M. Feenstra, *J. Appl. Phys.*, 1988, **64**, 4843–4852.
38 H. H. Radamson, K. B. Joelsson, W. X. Ni, J. Birch, J. E. Sundgren, L. Hultman and G. V. Hansson, *J. Cryst. Growth*, 1996, **167**, 495–501.
39 P. M. J. Marée, J. C. Barbour, J. F. van der Veen, K. L. Kavanagh, C. W. T. Bulle-Lieuwma and M. P. A. Viegers, *J. Appl. Phys.*, 1987, **62**, 4413–4420.
40 M. Clavel, P. Goley, N. Jain, Y. Zhu and M. K. Hudait, *IEEE J. Electron Devices Soc.*, 2015, **3**, 184–193.
41 M. B. Clavel, G. Greene-Diniz, M. Grüning, K. T. Henry, M. Kuhn, R. J. Bodnar and M. K. Hudait, *ACS Appl. Electron. Mater.*, 2019, **1**, 2646–2654.
42 D. P. Miller, J. E. Moore and C. Moore, *J. Appl. Phys.*, 1962, **33**, 2648–2652.
43 G. Schwuttke, *J. Appl. Phys.*, 1963, **34**, 1662–1664.
44 S. Chopra, M. C. Ozturk, V. Misra, K. McGuire and L. E. McNeil, *Appl. Phys. Lett.*, 2006, **88**, 202114.
45 J. Tersoff and F. LeGoues, *Phys. Rev. Lett.*, 1994, **72**, 3570.
46 M. K. Hudait, S. Bhattacharya, S. Karthikeyan, J. Zhao, R. Bodnar, B. Magill and G. Khodaparast, *J. Mater. Chem. C*, 2024, **12**, 14062–14073.
47 X. Lu, Z. Jiang, H. Zhu, X. Zhang and X. Wang, *Appl. Phys. Lett.*, 1996, **68**, 3278–3280.
48 E. Gaubas and J. Vanhellemont, *J. Electrochem. Soc.*, 2007, **154**, H231.
49 J. J. Sheng, D. Leonhardt, S. M. Han, S. W. Johnston, J. G. Cederberg and M. S. Carroll, *J. Vac. Sci. Technol. B*, 2013, **31**, 051201.
50 S. Deb and B. R. Nag, *J. Appl. Phys.*, 1962, **33**, 1604.
51 S. Johnston, K. Zaunbrecher, R. Ahrenkiel, D. Kuciauskas, D. Albin and W. Metzger, *IEEE J. Photovolt.*, 2014, **4**, 1295–1300.
52 K. L. Luke and L. J. Cheng, *J. Appl. Phys.*, 1987, **61**, 2282–2293.
53 E. Yablonovitch and T. J. Gmitter, *Solid State Electron.*, 1992, **35**, 261–267.
54 S. Bhattacharya, S. W. Johnston, S. Datta and M. K. Hudait, *ACS Appl. Electron. Mater.*, 2023, **5**, 3190–3197.
55 S. Bhattacharya, S. W. Johnston, R. J. Bodnar and M. K. Hudait, *ACS Appl. Electron. Mater.*, 2024, **6**, 4247–4256.
56 M. El Kurdi, H. Bertin, E. Martincic, M. de Kersauson, G. Fishman, S. Sauvage, A. Bosseboeuf and P. Boucaud, *Appl. Phys. Lett.*, 2010, **96**, 041909.

57 F. Murphy-Armando and S. Fahy, *J. Appl. Phys.*, 2011, **109**, 113703.
58 M. B. Clavel, F. Murphy-Armando, Y. Xie, K. T. Henry, M. Kuhn, R. J. Bodnar, G. A. Khodaparast, D. Smirnov, J. J. Heremans and M. K. Hudait, *Phys. Rev. Appl.*, 2022, **18**, 064083.
59 E. F. Schubert, in *Doping in III-V Semiconductors*, Cambridge University Press, Cambridge, 1993, p. 35, DOI: **10.1017/CBO9780511599828**.
60 J. Parsons, R. J. H. Morris, D. R. Leadley, E. H. C. Parker, D. J. F. Fulgoni and L. J. Nash, *Appl. Phys. Lett.*, 2008, **93**, 072108.